

Spectroscopy of argon fluoride and krypton fluoride exciplexes in rare gas matrices

C. Bressler, W. G. Lawrence, and N. Schwentner

Citation: *The Journal of Chemical Physics* **105**, 10178 (1996); doi: 10.1063/1.472731

View online: <http://dx.doi.org/10.1063/1.472731>

View Table of Contents: <http://scitation.aip.org/content/aip/journal/jcp/105/23?ver=pdfcov>

Published by the [AIP Publishing](#)

Articles you may be interested in

[Resolution of anomalies in the geometry and vibrational frequencies of monobromosilylene \(HSiBr\) by pulsed discharge jet spectroscopy](#)

J. Chem. Phys. **105**, 10189 (1996); 10.1063/1.472962

[Relaxation of highly vibrationally excited cycloheptatriene in liquids and gases studied by picosecond UV absorption spectroscopy](#)

AIP Conf. Proc. **364**, 148 (1996); 10.1063/1.50190

[Photoionization of raregas atoms studied by VUV fluorescence spectroscopy](#)

AIP Conf. Proc. **216**, 179 (1990); 10.1063/1.39949

[Laser generation of VUV radiation and spectra of rare gas excimers](#)

AIP Conf. Proc. **172**, 7 (1988); 10.1063/1.37484

[Fluorescence spectroscopy of ultrashortlived states of aromatic molecules](#)

AIP Conf. Proc. **172**, 718 (1988); 10.1063/1.37464



Spectroscopy of argon fluoride and krypton fluoride exciplexes in rare gas matrices

C. Bressler,^{a)} W. G. Lawrence,^{b)} and N. Schwentner

Institut für Experimentalphysik, Freie Universität Berlin, Arnimallee 14, D-14195 Berlin, Germany

(Received 29 July 1996; accepted 10 September 1996)

The spectroscopy of argon fluoride and krypton fluoride exciplexes in rare gas matrices is investigated using synchrotron radiation over the range of 50 to 600 nm. The diatomic Ar^+F^- and Kr^+F^- species are observed in excitation and emission spectra. Extensive vibrational progressions are observed in the excitation spectra and are used to determine the spectroscopic parameters of the ArF B state ($T_e=50233\text{ cm}^{-1}$, $\omega_e=415.5\text{ cm}^{-1}$, $\omega_e x_e=3.1\text{ cm}^{-1}$) and D state ($T_e=51738\text{ cm}^{-1}$, $\omega_e=476.7\text{ cm}^{-1}$, $\omega_e x_e=3.8\text{ cm}^{-1}$) and of the KrF B state ($T_e=39024\text{ cm}^{-1}$, $\omega_e=342.4\text{ cm}^{-1}$, $\omega_e x_e=2.0\text{ cm}^{-1}$) and D state ($T_e=44479\text{ cm}^{-1}$, $\omega_e=331.6\text{ cm}^{-1}$, $\omega_e x_e=1.4\text{ cm}^{-1}$). Lifetimes of 4 to 8 ns are measured for the diatomic emissions. A perturbed KrF species is observed which is identified in analogy to a similarly perturbed XeF species. Excitation spectra of the triatomic exciplexes Kr_2^+F^- and Ar_2^+F^- in neon are presented and described in terms of previous *ab initio* calculations. Emission and excitation of argon fluoride and krypton fluoride species in other matrices are presented. Large stimulated emission cross sections on the order of 10^{-16} cm^2 are determined for the diatomic $D\rightarrow X$ and $B\rightarrow X$ emissions, which, together with nonradiative relaxation processes within the B and D states of ArF that efficiently populate the $B(v=0)$ regardless of initial excitation, make ArF in neon a viable solid-state laser candidate. © 1996 American Institute of Physics. [S0021-9606(96)00947-6]

I. INTRODUCTION

Condensed phase excimer lasers may present an improvement over conventional gas phase excimer lasers. The solid medium offers the possibility of higher gain (per unit length) since the number density of excimer centers which can be generated in the solid is higher than in the conventional gas phase laser system. Since the rare gas host stabilizes the halogen atoms which are prepared in the initial photodissociation process, the pumping efficiency in the solid is higher. All of the pump energy is used to excite the RgX excimers, while in the gas phase laser a complete dissociation and pump cycle is required for every pulse. Successful operation of a solid state excimer laser has been demonstrated on the $B\rightarrow X$ (411 nm) and $C\rightarrow A$ (540 nm) transitions of XeF in an Ar crystal.¹ The gain per unit length of this system was found to be 2 orders of magnitude higher than conventional excimer lasers.² Extension to shorter wavelength has been demonstrated for the $D\rightarrow X$ transition of XeF in Kr at 302 nm,³ Ar at 286 nm,⁴ and Ne at 269 nm.⁵ Stimulated emission of KrF in Ar is hindered by the formation of $(\text{ArKrF})^*$,⁶ but line narrowing has been observed on the $B\rightarrow X$ transition at 256 nm.⁷ Excitation of the charge transfer state in fluorine atom doped rare gas solids typically leads to emission from Rg_2^+F^- triatomic excimers. The triatomic excimers are lower in energy than the Rg^+F^- diatomic excimers, and the high density of the solid ensures that rare gas atoms are available to form the triatomic.⁸ Transient absorptions of these triatomic excimers inhibit stimu-

lated emission processes.⁹ The transient absorptions are not observed for diatomic $\text{Rg}'^+\text{F}^-$ exciplexes which can be prepared in matrices codoped with atomic fluorine and a heavier rare gas. A lighter host gas, Rg , codoped with atomic fluorine and a heavier rare gas, Rg' , leads to formation of $\text{Rg}'\text{F}$ trapping sites. If the excited states of $\text{Rg}'\text{F}$ lie well below the excited states of the matrix, the guest remains largely uncoupled from the host. Formation of the $\text{Rg}'\text{F}$ dimers requires dissociation of the parent F_2 molecules with subsequent cage exit and migration of the F atom fragment. This photoinduced mobility, which is used to prepare high concentrations of $\text{Rg}'\text{F}$ species, is an advantage of fluorine atoms not observed for the heavier halogens. Efficient cage exit and photomobility has been observed in experiments^{6,10,11} and molecular dynamics (MD) simulations.^{12,13} Large photoinduced penetration depths of fluorine atoms into Ar matrices were confirmed recently in a "sandwich" matrix system.¹⁴ The $\text{Rg}'\text{F}$ content can be increased further by thermally activated migration of isolated F atoms which are efficiently trapped at the heavier Rg' atom within the matrix. The large dipole of the guest charge transfer state is solvated by the matrix while the ground state of the complex is not perturbed. The emissions observed for the $\text{Rg}'^+\text{F}^-$ excimers are red shifted from the gas phase, and this red shift is greater for the larger more polarizable matrices. Since neon has the largest ionization energy and is the least polarizable of the rare gasses, the guest host interaction is minimized in neon matrices.

The initial matrix isolation studies some rare gas fluoride exciplexes were done by Ault and Andrews¹⁵ and Goodman and Brus.¹⁶ The spectroscopy of matrix isolated XeF has recently been reported in more detail.¹⁷ The electronic states

^{a)}Present address: Molecular Physics Laboratory, SRI International, 333 Ravenswood Ave., Menlo Park, CA 94025.

^{b)}Also at: Department of Chemistry, Emory University, Atlanta, GA 30322.

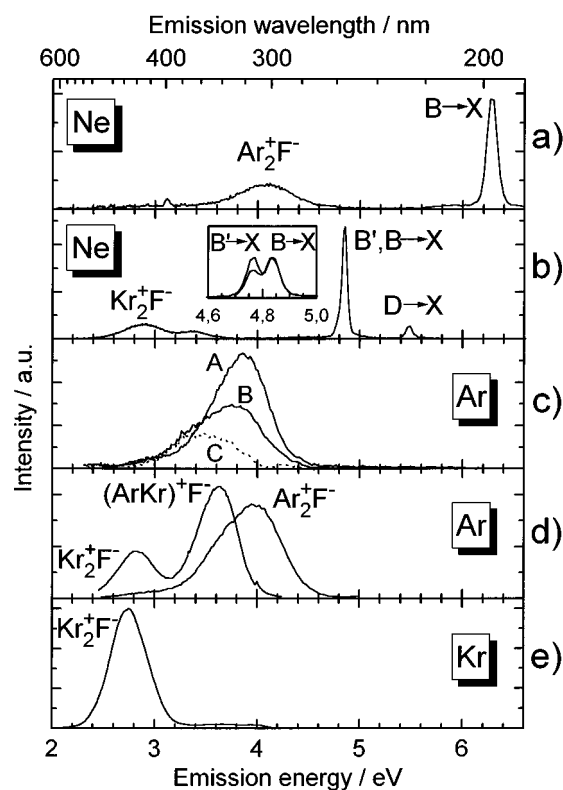


FIG. 1. Emission spectra of argon fluoride and krypton fluoride exciplexes in rare gas matrices following broadband photolysis of F_2 . (a) Emission from a matrix of F_2 :Ar:Ne (1:10:500) upon excitation at 7.3 eV. (b) Emission from a matrix of F_2 :Kr:Ne (2:1:500) upon excitation at 13.978 eV (F^*3s). The insert shows the change in the relative intensities of the $B' \rightarrow X$ and $B \rightarrow X$ emissions with further F_2 photolysis (see text). (c) Emission spectra from a matrix of F_2 :Ar (1:1000). Spectrum A emphasizes the $Ar_2^+F^-$ emission upon excitation at 7.3 eV. Spectrum B has contributions from both $Ar_2^+F^-$ and $Ar_6^+F^-$ upon excitation at 6.6 eV. Spectrum C is the difference of A and B and illustrates the $Ar_6^+F^-$ emission. (d) Emission spectra from a matrix of F_2 :Kr:Ar (1:1:1000). $Kr_2^+F^-$ and $(ArKr)^+F^-$ emission observed upon excitation at 4.77 eV and $Ar_2^+F^-$ emission observed upon excitation at 7.3 eV. (e) Emission from a matrix F_2 :Kr (1:1000) upon excitation at 4.8 eV.

of RgF dimers were calculated by Dunning and Hay^{18,19} and the electronic surfaces of the Rg_2F trimers were investigated by *ab initio*^{20,21} and diatomics in molecules (DIM)²² methods. Extension of these studies to excimers of F atoms with other rare gas atoms are of interest since the higher ionization energies of the lighter rare gas atoms leads to higher energies of the $Rg^+F^- \rightarrow RgF$ transitions.⁹ The VUV spectroscopy of F atoms in Ne matrices and the emissions of F_2 , Ne^+F^- , and F atom Rydberg states have been reported previously.^{23,24} This study presents the spectroscopic characterization of ArF and KrF excimers in the UV and VUV spectral regions, with a particular emphasis on excimers in neon matrices. The $B \rightarrow X$ and $D \rightarrow X$ emission and excitation spectra, the lifetimes of the excited states, and the stimulated emission cross sections are presented.

II. EXPERIMENT

These experiments were conducted at the 3m-NIM2 beamline at the synchrotron radiation facility, BESSY, in

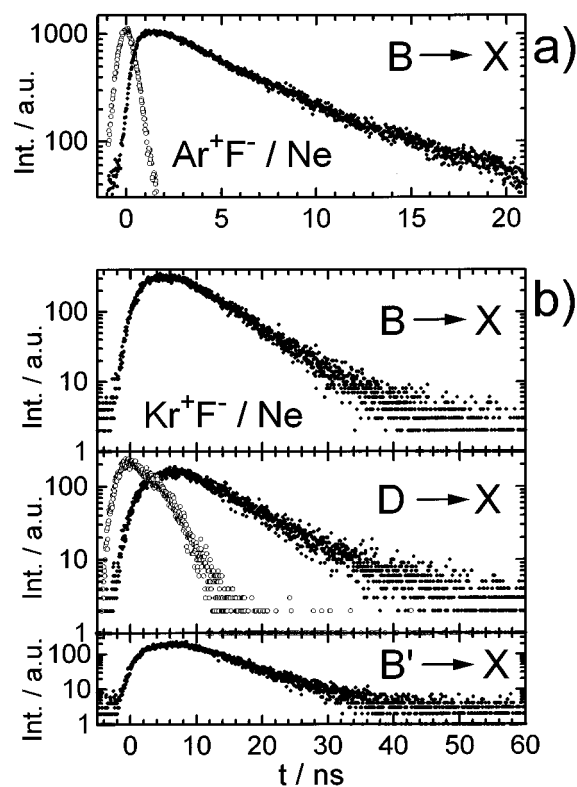


FIG. 2. Time resolved fluorescence of ArF and KrF dimers in neon matrices at 5 K. (a) $B \rightarrow X$ fluorescence monitored at 6.266 eV following excitation at 7.3 eV of a sample of original composition F_2 :Ar:Ne (2:1:500). (b) $Kr_2^+F^-$ fluorescence of the $B \rightarrow X$ emission monitored at 4.83 eV upon excitation at 4.96 eV, the $D \rightarrow X$ emission monitored at 5.47 eV upon excitation at 5.636 eV, the $B' \rightarrow X$ emission monitored at 4.75 eV upon excitation at 4.96 eV. The sample has an initial composition of F_2 :Kr:Ne (2:1:500). Open circles give the stray light response.

Berlin, Germany. Tunable radiation in the range of 50 to 300 nm is obtained by dispersing the synchrotron radiation using the 3 m normal incidence primary monochromator.²⁵ The output of the primary monochromator is focused to a 0.2×0.5 mm² spot on a LiF substrate which is cooled by a liquid helium flow cryostat to 4 K. The incoming photon flux of the 3m-NIM2 primary monochromator is more than 10^{12} photons/s within a typical bandwidth of 0.15 nm. Samples are premixed in a passivated UHV gas line and deposited by

TABLE I. Measured lifetimes, τ_m , in the Ne matrix, extrapolated gas phase values, τ_g , according to Eq. (4), and gas phase values, τ , from literature (all values in units of 10^{-9} s). Emission wavelength λ (in nm), line width $\Delta\nu$ (FWHM in meV) and stimulated emission cross sections, σ , (in 10^{-16} cm²) from Eq. (3).

	ArF ($B \rightarrow X$)	KrF ($B \rightarrow X$)	KrF ($D \rightarrow X$)	KrF ($B' \rightarrow X$)
τ_m	4.2	7.5	8.4	7.2
τ_g	5.5	9.4	10.9	9.4
τ	4.2 ^a	9.0 ^{b(6.7)}	12 ^a	...
λ	197.9	256.4	226.6	260.8
$\Delta\nu$	80	50	90	50
σ	0.8	1.2	0.4	1.2

^aReference 17.

^bReference 11.

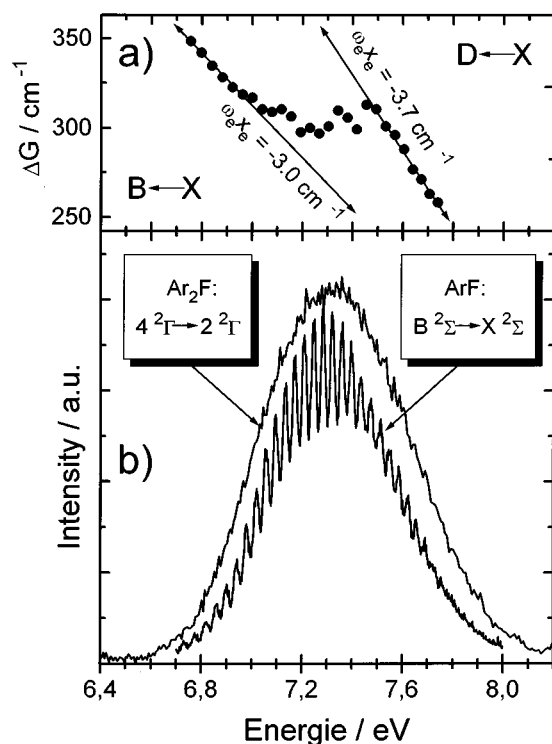


FIG. 3. Excitation spectra and peak spacings from a matrix of initial composition of $F_2:Ar:Ne$ (2:1:500) at 5 K. (a) Vibrational spacings, ΔG , versus excitation energy. The straight lines are used to indicate the difference in anharmonicity of the two progressions. The anharmonicity is derived from the Birge Spooner plots given in Fig. 5. (b) Excitation spectra of the $Ar^+F^- B \rightarrow X$ and the $Ar_2^+F^- 4^2\Gamma \rightarrow 1,2^2\Gamma$ emissions.

continuous flow onto the cooled substrate. Matrices of 0.1 to 10 μm thickness were prepared at a deposition rate between 1 and 40 nm/s. Rare gases from Linde were used at stated purity. Ne(99.9990%), Ar(99.9990%), Kr(99.998%). A 5% F_2/Ne mixture from Air-Liquide was used as the fluorine source. Emission spectra are recorded using a Czerny–Turner UV-VIS monochromator which provided a typical resolution of 1 nm, and a cooled XP2020Q photomultiplier tube.

Emission and excitation spectra were taken after photodissociation of matrix isolated F_2 . Broadband irradiation from the zeroth order of the primary monochromator is used as the photodissociation source. Time resolved measurements are taken in the single-bunch mode at BESSY, which provides pulse duration of about 400 ps and an interval of 208 ns between pulses. Scattered light from the primary excitation source is used to define the instrument resolution. Photon counting techniques, and a time to amplitude converter are used to achieve an instrument response of 700 ps (FWHM) and lifetime resolution of about 300 ps with deconvolution.

III. RESULTS

The emission spectra observed in these rare gas fluoride exciplexes are compiled in Fig. 1. Emission bands from matrices of argon and fluorine [Fig. 1(a)] and krypton and fluo-

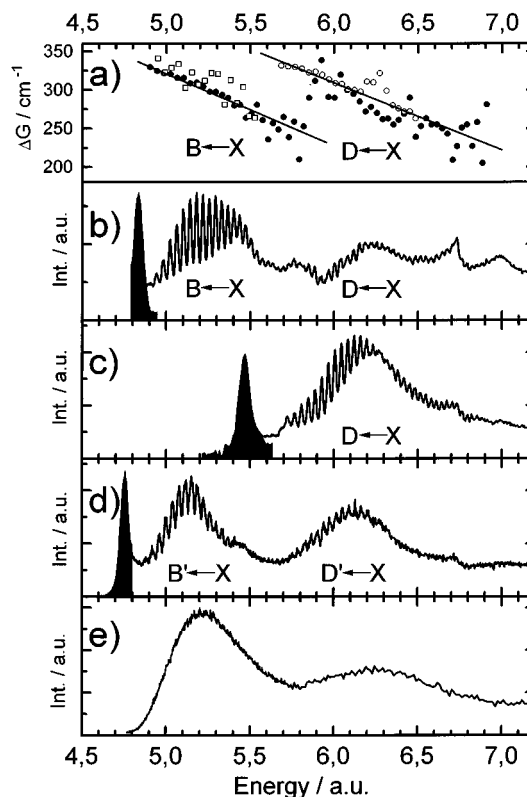


FIG. 4. Excitation spectra and peak positions from a matrix of initial composition of $F_2:Kr:Ne$ (2:1:500) at 5 K. (a) Vibrational spacing versus energy as in Fig. 3(a). (●) from $Kr^+F^- B \rightarrow X$ (○) $Kr^+F^- D \rightarrow X$ (□) from absorption data of Ref. 15. (b) Excitation spectrum of the $Kr^+F^- B \rightarrow X$ emission at 4.83 eV. (c) Excitation spectrum of the $Kr^+F^- D \rightarrow X$ emission at 5.47 eV. (d) Excitation spectrum of the $Kr^+F^- B' \rightarrow X$ emission at 4.75 eV. (e) $Kr_2^+F^- 4^2\Gamma \rightarrow 1,2^2\Gamma$ emission at 2.8 eV. The filled bands in (b), (c), and (d) are the emissions corresponding to each excitation spectrum.

rine [Fig. 1(b)] in Ne are shown. The emission lifetime profiles for all of the diatomic exciplex emissions of ArF [Fig. 2(a)] and KrF [Fig. 2(b)] are presented in Fig. 2. The stray light time dependence is given by the open circles and is used to characterize the instrument response. The derived lifetimes are given in Table I. Excitation spectra, in which the intensity of the emission band is recorded versus the energy of the exciting light, for the ArF $B \rightarrow X$ emission and of the $Ar_2^+F^- 4^2\Gamma \rightarrow 1,2^2\Gamma$ emissions in Ne matrices are presented in Fig. 3. Similarly, the excitation spectra of the three KrF emissions in Ne ($B \rightarrow X$, $B' \rightarrow X$, and $D \rightarrow X$) are presented together with the $Kr_2^+F^- 4^2\Gamma \rightarrow 1,2^2\Gamma$ in Fig. 4. The excitation spectrum of $Ar_2^+F^-$ in an Ar matrix is given in Fig. 5, and the excitation spectrum of $Kr_2^+F^-$ emission in a krypton matrix is shown in Fig. 6. The details of each emission system are reported in the following sections.

A. ArF in Ne

Irradiation of an F_2 and Ar-doped neon matrix with broadband radiation from the zeroth order of the primary monochromator leads to F_2 dissociation and subsequent trapping of fluorine atoms near argon. The emission spectrum of a sample of original composition $F_2:Ar:Ne$ (1:10:500) is

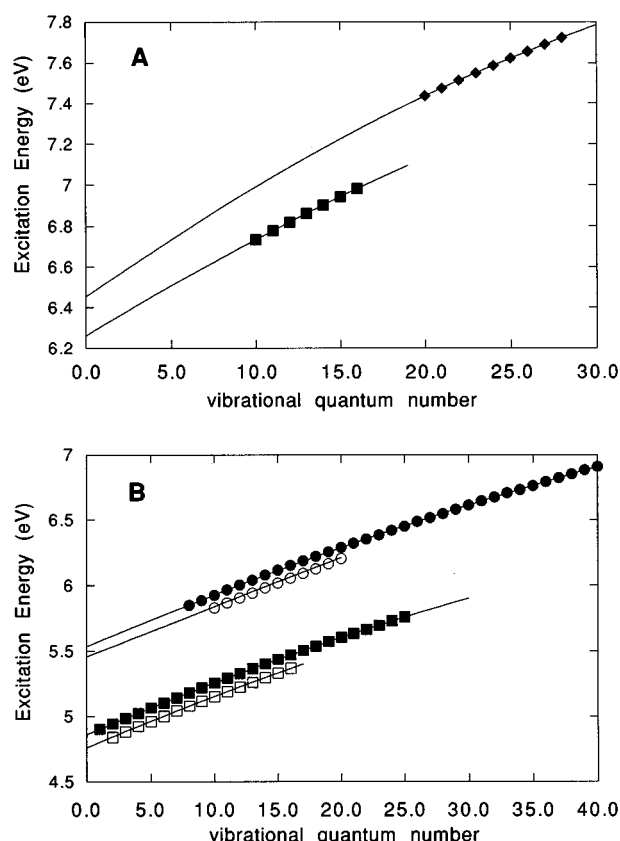


FIG. 5. Birge-Spencer plots of the vibrational bands observed in the ArF and KrF excitation spectra. (A) (■) Ar^+F^- B state, (◆) Ar^+F^- D state. (B) (■) Kr^+F^- B state, (□) Kr^+F^- B' state, (●) Kr^+F^- D state, (○) Kr^+F^- D' state.

shown in Fig. 1(a), and emphasizes the triatomic exciplex emission at 4.12 eV. Emission spectra of the diatomic exciplexes are recorded in lower concentration matrices, typically 1:2:500 ($\text{F}_2:\text{Ar}:\text{Ne}$). The emission observed at 6.266 eV is assigned to the ArF $B \rightarrow X$ transition and is red shifted by 160 meV from the gas phase emission at 6.42 eV. The excitation spectrum of this emission is given in Fig. 3(b) and shows what appears as a single Franck-Condon envelope. However, when the energy difference between successive peaks is plotted against excitation energy, as shown in the top of Fig. 3, a pronounced irregularity is observed between 7.2 and 7.4 eV. This irregularity is the result of having two distinct overlapping progressions in the excitation spectrum with maxima near 7.3 and 7.5 eV. The energy difference of 200 meV between the maxima of the two progressions is close to the 178 meV spin orbit splitting of Ar^+F^- .¹⁸ The Birge-Spencer plot for the two states is shown in Fig. 5. The lower energy progression, which is observed between 6.7 and 7.1 eV has an anharmonicity of 3.0 cm^{-1} , while the higher energy progression, which is observed between 7.4 and 7.8 eV has an anharmonicity of 3.7 cm^{-1} . The remaining peak positions are distorted by the overlapping bands. The energies of the vibrational bands and ΔG values are listed in Table II. The excitation spectrum in Fig. 3(b) includes excitation to both the B and D states, yet only the $B \rightarrow X$ emis-

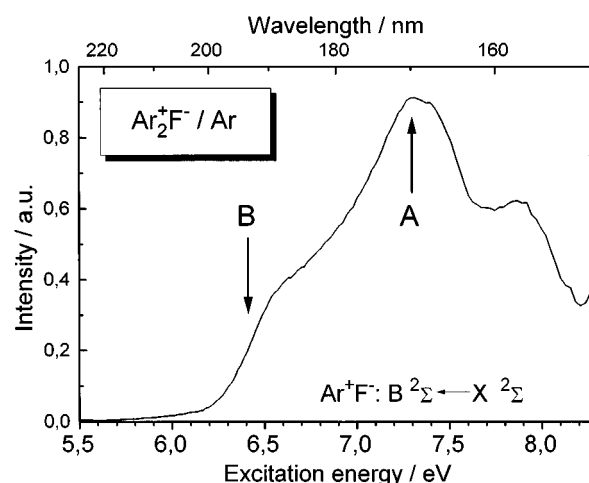


FIG. 6. Excitation spectra recorded by monitoring the emission at 3.93 eV from a matrix of $\text{F}_2:\text{Ar}$ (1:1000). Emission from both Ar_2^+F^- and Ar_6^+F^- are observed at 3.73 eV. A and B denote the excitation energies for the corresponding emission spectra in Fig. 1(c).

sion is observed. This implies rapid nonradiative relaxation of the D state population into the B state. The lifetime of the $B \rightarrow X$ emission is 4.2 ns while the calculated $D \rightarrow X$ lifetime is significantly longer (Table I). The weak broadband on the red side of the $B \rightarrow X$ transition near 5.8 eV is attributed to the $B \rightarrow A$ transition. This emission is broad and red shifted from the $B \rightarrow X$ since the lower state of the transition is more repulsive. In contrast to Xe^+F , the $C \rightarrow A$ and $D \rightarrow X$ transitions cannot compete with the nonradiative relaxation into the bottom of the low lying B state.

The relative intensities of the 6.27 eV $B \rightarrow X$ emission and the 4.12 eV emission is dependent on the argon content of the matrix. This emission at 4.12 eV is assigned to the $\text{Ar}_2^+\text{F}^- 4^2\Gamma \rightarrow 1,2^2\Gamma$ transition which is red shifted from the gas phase emission by 230 meV. The red shift is the result of the solvation of the large dipole of the Ar_2^+F^- exciplex by the neon matrix. The width of this transition [FWHM of 500 meV (35 nm)] is characteristic of bound ($4^2\Gamma$) to dissocia-

TABLE II. Energies, E_a , of maxima in the excitation spectra of ArF in Ne (Fig. 3) and vibrational energy spacing, ΔG , with assignment of to vibrational quanta v' of B from 10 to 17 and of D from 20 to 28.

v'	E_a/eV	$\Delta G/\text{cm}^{-1}$	v'	E_a/eV	$\Delta G/\text{cm}^{-1}$
10 (B)	6.7335	348	...	7.2843	301
11	6.7767	342	...	7.3216	310
12	6.8191	335	...	7.3600	306
13	6.8606	328	...	7.3979	299
14	6.9013	323	20 (D)	7.435	313
15	6.9413	319	21	7.4738	311
16	6.9808	317	22	7.5123	301
17	7.0201	311	23	7.5496	296
...	7.0586	309	24	7.5863	288
...	7.0969	311	25	7.6220	277
...	7.1354	306	26	7.6563	271
...	7.1734	298	27	7.6899	263
...	7.2103	300	28	7.7225	...
...	7.2475	297			

tive ($1,2\ ^2T$) transitions. The excitation spectrum of the Ar_2^+F^- is shown in Fig. 3(b) together with the excitation spectrum of the diatomic exciplex. Intense fluorescence from the $B \rightarrow X$ emission also showed up with excitation of the atomic Ar bands at 12.6 and 12.8 eV, and upon excitation of the atomic F band ($3s$) at 13.95 eV. Near 17 eV the neon matrix absorptions begin and the contribution of the Ne excitons was observed.

B. KrF in Ne

Four emissions were observed following photodissociation of fluorine in neon matrices doped with F_2 and Kr. Samples with concentrations of $\text{F}_2\text{:Kr:Ne}$ (500:2:1) and (100:2:1) were prepared to vary the relative KrF and Kr_2F concentrations. The insert of Fig. 1(b) shows two spectra at low-dopant concentration, while the complete emission spectrum of Fig. 1(b) was obtained in a sample at higher concentration. The strong emission at 4.8 eV consists of two bands centered at 4.83 eV (256.6) and 4.75 eV (260.8 nm). These two bands are resolved in the insert to Fig. 1(b). The band at 4.83 eV has previously been assigned to the $B \rightarrow X$ transition of Kr^+F^- .⁶ This emission is red shifted by 180 meV from the gas phase value of 5.00 eV (248 nm).^{9,26} The excitation spectrum of the $B \rightarrow X$ emission shows two long vibrational progressions with Franck–Condon envelopes centered at 5.25 and 6.2 eV [Fig. 4(b)]. The plot of the energy difference between successive peaks with excitation energy, which is given above the excitation spectrum, shows two vibrational progressions. From the Birge–Sponer plot of vibrational spacing versus vibrational quantum number shown by the solid squares in Fig. 5(b), an anharmonicity of 1.87 cm^{-1} is derived for the lower energy vibrational progression between 4.9 and 5.8 eV. More than 25 vibrational levels are observed in this progression, which has previously been partially recorded in the absorption by Ault and Andrews.¹⁵ The open squares in Fig. 4(a) indicate the ΔG values observed in the absorption spectra. Another vibrational progression which is assigned to the $D \leftarrow X$ transition, appears at higher energies between 5.9 and 7 eV. About 30 vibrational levels are identified in this progression. In the region between 5.6 and 5.9 eV the $D \leftarrow X$ and $B \leftarrow X$ excitation bands overlap as indicated by the filled circles in Fig. 4(a). The contribution of the D state excitation to the $\text{KrF } B \rightarrow X$ emission is evident in Fig. 4(b) and demonstrates that nonradiative relaxation from $D\ ^2\Sigma \rightarrow B\ ^2\Sigma$ is quite efficient. The $D \rightarrow X$ emission at 5.47 eV (226.6 nm) is observed upon direct excitation of the D state and is shown in Fig. 4(c). This is in contrast to direct excitation of the D state of ArF which does not produce $D \rightarrow X$ emission since the nonradiative relaxation is much faster than radiative relaxation. The plot of the excitation spectrum of the D state observed by monitoring the $D \rightarrow X$ emission shows the same vibrational progression as the D state observed by monitoring the $B \rightarrow X$ emission [open and filled circles in Fig. 4(a)]. Lower vibrational states of the D state are observed by monitoring the $D \rightarrow X$ emission since there is no interference from the B state excitation spectrum.

Another emission band at 4.75 eV, which is very near

the $\text{KrF } B \rightarrow X$ emission at 4.83 eV, is shown in the shaded region in Fig. 4(d). The excitation spectrum of this emission [Fig. 4(d)] is very similar to the $\text{KrF } B \leftarrow X$, and the Birge–Sponer plots in Fig. 5(b) demonstrate that the vibrational progressions yield frequencies which are identical to those observed for the $B \leftarrow X$ transition. A careful inspection of the individual bands show that the vibrational levels in the excitation spectrum of the 4.75-eV emission are slightly red shifted to those assigned to the B state excitation. The 4.75-eV emission is from a state with very similar properties to the B state and is denoted as B' . It is also observed that the intensity of the $B' \rightarrow X$ emission grows at a different rate than the $B \rightarrow X$ and $D \rightarrow X$ emissions during the F_2 dissociation. (The intensity ratio of D and B is always the same.) This relative intensity variation between the $B' \rightarrow X$ and $B \rightarrow X$ is illustrated in the inset to Fig. 1(b). The spectrum with the lower irradiation dosage shows a lower relative intensity of $B' \rightarrow X$ emission. The other spectrum presented is upon further irradiation. A similar emission pair has been observed for XeF in rare gas matrices. These emissions are assigned as B and B^* .¹⁷ In the xenon fluoride case the B^* emission is assigned to a XeF dimer with a second F atom nearby. The F atom perturbation causes a spectral shift and increases the vibrational spacing by 30%. We postulate that the $B' \rightarrow X$ emission and $B' \leftarrow X$ excitation are due to a similar perturbation. However, in this case the vibrational spacing is the same within the experimental accuracy, and only a shift in the transition energy is observed. A similar higher energy excitation is assigned to the D' state in analogy to the B' state. The vibrational levels of the D' excitation are given by the open circles in the Birge–Sponer plots of Fig. 5. The D' state is also red shifted from the D state. The line positions and energy spacings of the diatomic transitions are listed in Table III.

Neon matrices with higher Kr concentration of 2:1:100 ($\text{Kr:F}_2\text{:Ne}$) show a stronger emission at 2.88 eV (430 nm) in Fig. 1(b). This emission is assigned to Kr_2^+F^- , and the intensity of the emission is dependent on the krypton dimer trapping probability. A weaker emission is observed at 3.38 eV. The intensity ratio of the primary Kr_2^+F^- emission at 2.88 to the blue shoulder at 3.38 is 3:1. This intensity ratio is independent of matrix concentration. The excitation spectrum of the Kr_2^+F^- at 2.88 eV is shown in Fig. 4(e), and is composed of two broad structureless bands. The blue shoulder is present at the same intensity ratio upon excitation into either band, and this suggests a common emitting state for both emissions.

C. ArF and KrF in Ar, KrF in Kr

In Fig. 1(c) the asymmetric emission band, denoted B , is observed in an argon matrix after F_2 dissociation with 6.42 eV (193 nm). Previous studies¹⁰ with time gated detection show that this emission is a convolution of two bands, one centered at 3.49 eV (355 nm) and another at 3.54 eV (315 nm). The higher energy band is assigned to Ar_2^+F^- emission, while the lower band is assigned to an $(\text{Ar}_6)^+\text{F}^-$ center.¹⁰ The excitation spectrum of the overlapping emissions, shown

TABLE III. Energies, E_a , of maxima in the excitation spectra of KrF in Ne (Fig. 4) for the $B \rightarrow X$, $B' \rightarrow X$, and $D \rightarrow X$ emissions. Vibrational assignments are listed together with the vibrational energy spacing, ΔG .

v'	$B \rightarrow X$ E_a/eV	$\Delta G/\text{cm}^{-1}$	v'	$B' \rightarrow X$ E_a/eV	$\Delta G/\text{cm}^{-1}$	v'	$D \rightarrow X$ E_a/eV	$\Delta G/\text{cm}^{-1}$
1	4.9024	330						
2	4.9433	325	2	4.8404	328			
3	4.9836	322	3	4.8811	329			
4	5.0235	321	4	4.9218	328			
5	5.0633	316	5	4.9625	318			
6	5.1025	316	6	5.0019	316			
7	5.1417	309	7	5.0411	307			
8	5.1800	310	8	5.0792	304			
9	5.2184	305	9	5.1169	294			
10	5.2562	298	10	5.1533	286			
11	5.2932	298	11	5.1888	286			
12	5.3301	294	12	5.2242	288			
13	5.3666	290	13	5.2600	297			
14	5.4025	280	14	5.2968	289			
15	5.4373	281	15	5.3326	290			
16	5.4721	264	16	5.3686	284			
17	5.5048	269	...	5.6084	199			
18	5.5382	281	...	5.6330	236			
19	5.5730	261	...	5.6623	245			
20	5.6054	236	...	5.6927	185			
21	5.6346	257	...	5.7156	311			
22	5.6665	249	...	5.7542	275			
23	5.6978	265	...	5.7883	330			
24	5.7302	239	(D')	5.8292	303	4	5.6842	332
25	5.7599	259		5.8667	305	5	5.7254	331
26	5.7920	210		5.9046	307	6	5.7664	330
...	5.8180	253		5.9426	300	7	5.8073	328
8 (D)	5.8494	290		5.9798	307	8	5.8480	323
9	5.8853	312		6.0179	294	9	5.8881	324
10	5.9240	339		6.0543	293	10	5.9282	320
11	5.9660	291		6.0907	288	11	5.9679	314
12	6.0021	290		6.1263	311	12	6.0068	309
13	6.0381	320		6.1649	305	13	6.0452	308
14	6.0778	300		6.2027	288	14	6.0833	301
15	6.1150	295		6.2384	278	15	6.1207	300
16	6.1515	285		6.2729	329	16	6.1579	298
17	6.1869	272		6.3137	334	...	6.1948	311
18	6.2206	278		6.3551	6.2334	310
19	6.2551	270				...	6.2718	322
20	6.2885	262				...	6.3117	299
21	6.3210	263				22	6.3488	280
22	6.3536	255				23	6.3835	276
23	6.3852	261				24	6.4177	272
24	6.4176	269				25	6.4515	272
25	6.4510	290				26	6.4852	263
26	6.4869	239				27	6.5178	251
27	6.5165	253				28	6.5489	250
28	6.5479	263				29	6.5799	256
29	6.5805	255				30	6.6116	254
30	6.6121	255				31	6.6431	245
31	6.6438	250				32	6.6735	245
32	6.6747	243				33	6.7039	235
33	6.7049	209				34	6.7330	238
34	6.7308	227				35	6.7625	239
35	6.7589	251				36	6.7922	242
36	6.7901	255				37	6.8222	245
37	6.8217	227				38	6.8525	211
38	6.8498	258				39	6.8787	226
39	6.8818	205				40	6.9067	...
40	6.9072	281						
41	6.9421	...						

in Fig. 6, has a shoulder at 6.6 eV and a maximum at 7.3 eV. The $(\text{Ar}_6)^+\text{F}^-$ emission contribution in Fig. 1(c) (spectrum A) is significantly reduced upon excitation at the 7.3-eV maximum in Fig. 6 (indicated by arrow A). This excitation band centered around arrow A is attributed to the Franck–Condon maximum of the Ar_2^+F^- excitation. Excitation on the red side of the shoulder (indicated by arrow B in Fig. 6) enhances the $(\text{Ar}_6)^+\text{F}^-$ at 3.2 eV in spectrum B of Fig. 1(c). The $(\text{Ar}_6)^+\text{F}^-$ emission cannot be completely isolated by appropriate choice of excitation since the excitation maximum of $(\text{Ar}_6)^+\text{F}^-$ rides on the red wing of the Ar_2^+F^- excitation. Subtraction of spectra A and B in Fig. 1(c) produces (upon normalization of spectrum B) spectrum C, the emission band of $(\text{Ar}_6)^+\text{F}^-$. This is consistent with the line shape observed in Ref. 10. Spectrum A is predominately Ar_2^+F^- $4^2\Gamma \rightarrow 1,2^2\Gamma$ emission, and spectrum C is predominately $(\text{Ar}_6)^+\text{F}^-$ emission. The third excitation feature in Fig. 6 near 7.9 eV probably originates from OH contaminants which are produced by photodissociation of H_2O . The OH emission band centered at 3.64 eV cannot be separated from the argon fluoride emissions, and the excitation spectrum of OH in argon has a maximum in this region.²⁷

The emission spectrum from an argon matrix codoped with F_2 and Kr at typical concentrations 1:1:1000 (Kr: F_2 :Ar) is shown in Fig. 1(d). Excitation at 7.3 eV produces the Ar_2^+F^- emission described in the previous section. Excitation at lower energies between 4.7 and 5.9 eV produces two emissions which are assigned to the Kr_2^+F^- triatomic and to a mixed triatomic $(\text{ArKr})^+\text{F}^-$.⁶ The excitation spectrum of the mixed triatomic $(\text{ArKr})^+\text{F}^-$ emission contains a vibrationally resolved progression assigned to the $B \leftarrow X$ ($v'=0$ to 10) transition of Kr^+F^- , and a structureless envelope of the $D \leftarrow X$ transition (not shown). These observations are in agreement with previously reported excitation spectra⁶ and absorption spectra.¹⁰

Photodissociation of F_2 in a krypton matrix results in only one emission band at 2.88 eV [Fig. 1(e)] which is assigned to Kr_2^+F^- .⁶ The dominant excitation is a broad structureless band centered at 4.8 eV [spectra (a) and (c) in Fig. 7]. This excitation spectrum is not the same as the excitation spectrum reported in Ref. 6. The previously reported excitation spectrum consists of three bands at 275 nm (4.5 eV), 250 nm (4.9 eV), and 232 nm (5.3 eV), and the 4.9 eV and 5.3-eV bands are assigned to excitation into the B and D states, respectively, of $\text{Kr}+\text{F}^-$. The dominant 4.5-eV band is assigned to excitation of a delocalized Kr_n^+F^- complex. It is also proposed that the delocalized state is accessible only for an F atom in a tight octahedral or tetrahedral interstitial site. In these sites the potential minimum of the F atom is at the center in the Kr cage. The potential minimum for the F atom in the krypton substitutional site is far from the center of the cage, and breaks the symmetry required for the excitation of the delocalized state.⁶ In our present measurements, a transient feature at 4.5 eV is observed in the Kr_2^+F^- excitation spectrum [marked by (I) in spectrum (b) of Fig. 7]. Broadband irradiation of an F_2/Kr matrix with no previous irradiation history leads to the excitation spectrum labeled a in Fig. 7. Additional wavelength selected irradiation at 4.5

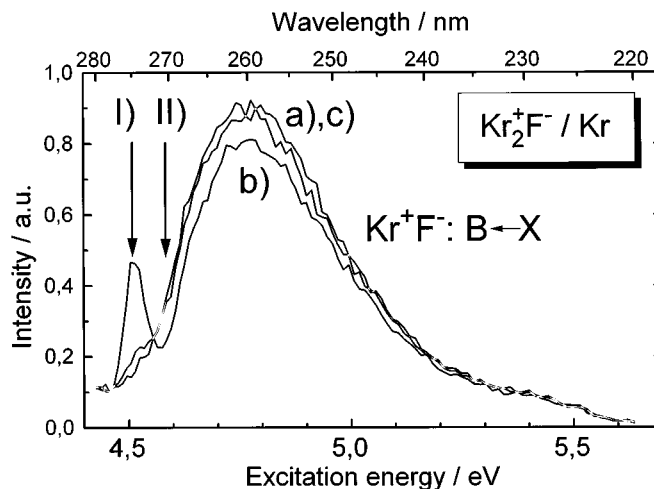


FIG. 7. Excitation spectra recorded by monitoring the Kr_2^+F^- $4^2\Gamma \rightarrow 1,2^2\Gamma$ emission at 2.74 eV from a matrix of $\text{F}_2:\text{Kr}$ (1:2000). (a) Excitation spectrum recorded after broadband photolysis of F_2 . (b) Excitation spectrum recorded after additional irradiation at 4.5 eV (arrow I). (c) Excitation spectrum recorded after additional irradiation at 4.6 eV.

eV produces the new excitation feature observed in the spectrum labeled (b) in Fig. 7. Excitation into the 4.5 eV feature produces an emission spectrum which is identical to the emission observed upon excitation into the 4.8-eV band. The new excitation is photobleached upon irradiation at energies greater than 4.6 eV. This process is reversible, and the 4.5-eV feature can be regenerated by excitation at 4.5 eV and bleached by higher energy excitation. This bleaching/regeneration process may be explained in terms of the previous assignment of the 4.5-eV excitation to the interstitial F atom excitation. Irradiation at 4.5 eV excites the interstitial F atoms which emit at 2.88 eV and produce some F atoms which are trapped in interstitial sites. Irradiation at energies above 4.6 eV excites interstitial F atoms but depletes the F atoms in interstitial sites. These F atoms must relax in the more stable substitutional site or defect sites. Other differences in the excitation spectra may be attributable to the type and distribution of sites formed in the preparation of the matrix.

IV. DISCUSSION

A. Diatomic exciplexes in neon

The diatomic rare gas fluorides, ArF and KrF , are formed in matrices by broadband UV irradiation of neon matrices doped with fluorine and either Ar or Kr. Emission and excitation spectra are observed for both argon fluoride and krypton fluoride. All of the diatomic emissions are composed of a single broad feature which does not change upon excitation into different vibrational levels of the excited state. The insensitivity to initial excitation implies that the emission is observed after fast relaxation into the lowest vibrational level of the excited state. In both ArF and KrF the B state potential minimum is at shorter internuclear separation than that of the ground state and emission terminates on the inner wall of the ground state potential above the disso-

ciation threshold. The minimum of the ArF ground state $X(1/2)$ potential has been measured in beam scattering experiments to be 3.31 \AA ,²⁸ while *ab initio* calculations predict a potential minimum of 2.31 \AA for the B state.¹⁸ The width of the ArF $B \rightarrow X$ emission is defined primarily by the shape of the inner wall of the ground state potential in the bound to repulsive transition. The high-energy edge of the emission spectrum is used to set an upper limit on the assignment of the vibrational level of the first transition observed in the excitation spectrum since the ν_{00} transition cannot be at lower energy than the highest energy emission. The center of the emission is at 6.266 eV and has a width of 80 meV , therefore the ν_{00} transition must be greater than 6.186 eV . From the assignment of the first observed transition to $\nu' = 9$, and the fit to the Birge–Sponer plot, a ν_{00} of 6.309 eV is derived. The frequency and anharmonicity of the B state with this assignment are 409 cm^{-1} and 3.1 cm^{-1} . T_e is derived from the ν_{00} by

$$T_e = \nu_{00} - \omega'_e/2 + \omega_e x'_e/4 + \omega''_e/2. \quad (1)$$

We have included only the first two terms, ω'_e and $\omega_e x'_e$, in the expansion of the upper state and the first term ω''_e , in the shallow lower state. A frequency of 43 cm^{-1} is derived from the ArF ground state potentials,²⁹ and a T_e of 6.286 eV is found.

The Birge–Sponer plot in Fig. 5(a) reveals two distinct vibrational progressions. The second vibrational progression is assigned to the ArF $D(^2P)$ state excitation spectrum. The energy difference at the asymptote of the D and B state is 178 meV and is defined by the spin orbit splitting of the $^2P_{1/2}$ and $^2P_{3/2}$ states of Ar^+ . The minimum of the D state potential can be approximated by adding the Ar^+ spin orbit splitting to the minimum of the B state potential. *Ab initio* calculations predict a splitting of 270 meV between the B and D states at the minima.¹⁸ This approximation gives a T_e of 6.463 eV and implies an assignment of $\nu' = 20$ to the first clearly observed transition of the D state. Based on this assignment, a frequency of 476.7 cm^{-1} and anharmonicity of 3.8 cm^{-1} are derived.

Similar arguments are used to determine the vibrational assignment of the KrF B state in neon. The emission of the KrF B state is centered at 4.830 eV and has a width of $\sim 25 \text{ meV}$. The potential minimum calculated for the KrF B state is 2.51 \AA ,¹⁸ and the minimum in the ground state is 2.84 \AA .²⁸ While the difference between the potential minima in ArF is $\sim 1 \text{ \AA}$, the difference in the potential minima of KrF is only $\sim 0.3 \text{ \AA}$. This change in the relative positions in the potential minima is reflected in the reduced width of the KrF $B \rightarrow X$ emission. The first observed transition in the KrF B state excitation spectrum is assigned to the $\nu' = 1 \leftarrow \nu'' = 0$ transition and gives a $\nu_{00} = 4.849 \text{ eV}$. The fit to the Birge–Sponer plot yields an ω_e and $\omega_e x_e$ of 342.4 cm^{-1} and 2.0 cm^{-1} . The peak of the emission of the KrF D state is observed at 5.470 eV and is about 60 meV wide. Assignment of the first observed transition at 5.684 eV to the $\nu' = 4 \leftarrow \nu'' = 0$ yields a ν_{00} of 5.525 eV with a frequency of 331.6 cm^{-1} and an anharmonicity of 1.35 cm^{-1} . The difference between the minima of the B and D state potentials is 676 meV and is

TABLE IV. Spectroscopic constants of the diatomic ArF and KrF excited states and comparison to gas phase values.

		T_e/eV	$\Delta E_d/\text{meV}$	ω_e/cm^{-1}	$\omega_e x_e/\text{cm}^{-1}$
Ar^+F^-					
$B\ ^2\Sigma$	gas	6.30		390	2.7
	Ne	6.278	−40	415.5	3.1
$D\ ^2\Pi$	gas	6.57		402 ^a	4.0
	Ne	6.414 ^b	−40	476 ^a	3.8
Kr^+F^-					
$B\ ^2\Sigma$	gas	4.93		339	1.7
	Ne	4.838		342 ^a	2.0
$B'\ ^2\Sigma$	Ne	4.737		340 ^a	2.0
$D\ ^2\Pi$	gas	5.55		352	2.7
	Ne	5.514		331.6 ^a	1.35
$D'\ ^2\Pi$	Ne	5.425		314.5 ^a	0.5

^aEstimated by extrapolation.

^b $T_e(D) = T_e(B) + \Delta_{so}(\text{Ar})$.

very close to the spin orbit splitting of Kr^+ which is 666 meV . Spectroscopic parameters for all of the diatomic states observed including the KrF B' state are listed in Table IV.

B. Triatomic exciplexes in neon

The Ar_2F and Kr_2F triatomic emissions in neon are observed at 4.12 and 2.88 eV , respectively. The relative intensities of the triatomic emission to the diatomic emission is dependent on the guest rare gas concentration. Higher guest rare gas concentrations increase the relative intensity of the triatomic emission. This concentration dependence is attributed to the statistical distribution of monomer and dimer trapping sites.

The *ab initio* calculations of Wadt and Hay²⁰ on the electronic states of Ar_2F and Kr_2F are quite useful in interpreting the observed excitation and emission spectra. The Ar_2F emissions are assigned to $4^2\Gamma \rightarrow 1,2^2\Gamma$ transition. *Ab initio* calculations show that the $4^2\Gamma$ state is bound by 0.6 eV with respect to $\text{Ar}^+\text{F}^- + \text{Ar}$ and is the only bound state which correlates to $\text{Ar}(^1S) + \text{Ar}^+(^2P) + \text{F}^-(^1S)$. Transitions are expected to both $1^2\Gamma$ and $2^2\Gamma$ lower surfaces. The calculations indicate that these two surfaces are separated by 0.12 eV at the minimum geometry of the $4^2\Gamma$ surface, and the broad bound to repulsive emissions will not be distinguishable. The potential surfaces of the Kr_2F are quite similar and the same $4^2\Gamma \rightarrow 1,2^2\Gamma$ emissions are observed.

Vertical excitation of the Kr_2F Van der Waals complex at the ground state geometry can access the $4^2\Gamma$ state which correlates to $\text{Kr}(^1S) + \text{Kr}^+\text{F}^-(^2\Sigma)$ and the 5 and $6^2\Gamma$ states which are nearly degenerate and correlate to $\text{Kr}(^1S) + \text{Kr}^+\text{F}^-(^2\Pi)$. At the ground state geometry the splitting between the $4^2\Gamma$ and $5,6^2\Gamma$ surfaces is defined primarily by the spin orbit splitting of $\text{Ar}^+(^2P)$. The two broad excitation features in Fig. 4(e) are assigned to the $4^2\Gamma$ excitation at 5.2 eV and to the $5,6^2\Gamma$ excitation near 6.5 eV . Emission is only observed from the $4^2\Gamma$ state which implies rapid nonradiative relaxation of the population in the dissociative $5,6^2\Gamma$ to the bound $4^2\Gamma$ well. The potential surfaces presented by Wadt and Hay show that $5,6^2\Gamma$ surfaces are weakly dissociative, while the $4^2\Gamma$ surface is bound by 0.5 eV relative to the

$\text{Kr}^+\text{F}^- (^2\Sigma) + \text{Kr} (^1S)$ limit. The vibrational structure in the excitation is washed out by the large anharmonicity and the density of modes in the $4^2\Gamma$ surface at the ground state equilibrium separation. Similar arguments are used to describe the Ar_2^+F^- excitation; however, the excitation bands of the $4^2\Gamma$ and $5,6^2\Gamma$ states overlap.

The similarity of the structureless Rg_2^+F^- excitation bands to the Frank–Condon envelopes of the B and D state Rg^+F^- excitations [Fig. 3(b), Figs. 4(b), 4(e)] invites an alternative assignment of the triatomic excitation spectra. The similarity of the diatomic and triatomic excitation spectra suggests that the Rg^+F^- charge transfer state is initially populated and undergoes rapid crossing to the $4^2\Gamma$ Rg_2^+F^- potential. The short lifetime of the initially populated state results in the loss of vibrational structure, but the excitation profile is defined by the curvature of the diatomic state. Since we do not have specific information about the shape of the triatomic surface in the excitation region, or a detailed description of the diatomic-triatomic coupling, we prefer the simpler mechanism of direct excitation of the triatomic exciplex.

C. Matrix shifts

The emission line centers of the rare gas fluoride charge transfer complexes in matrices are observed at lower energies than in the gas phase. Gas phase to matrix red shifts, ΔE_a , of 40 to 70 meV are observed in absorption for the KrF and ArF diatomic exciplexes in neon matrices, and these values are listed for all of the observed emissions in Table IV. These matrix shifts are attributed to the solvation of the upper charge transfer state which has a large dipole moment, while the neutral ground state is not affected by the matrix solvation. The red shift is described by the polarization energy induced by the large change in dipole, $\Delta\mu$, in the charge transfer transitions, and is given by^{8,30,31}

$$\Delta E_a = \frac{8(\epsilon - 1)\Delta\mu^2}{(2\epsilon + 1)d^3}, \quad (2)$$

where ϵ is the dielectric constant of the matrix, and d is the diameter of the Onsager cavity. This diameter of the cage in which the dipole of the dimer is embedded is not well defined. Since the energy shift is proportional to d^{-3} , there is ambiguity in the application of Eq. (2). The ΔE values are quite small and agree well with the 62 meV derived for the $B \rightarrow X$ transition of XeF in Ne.¹⁷ The dipole moments for all the transitions are about 10 D and there is no systematic correlation of the cavity diameter with the size of the dimer in rare gases from ArF to XeF . Cavity diameter values between 9.2 and 11.1 Å are obtained for $\Delta E_a = 70$ and 40 meV, respectively, given an $\epsilon = 1.24$ for Ne. These values exceed the geometrical size of the dimers, and the nearest-neighbor distance for Ne, which are required for this continuum model. These values are quite large relative to the typical values around $d = 7$ Å.^{17,31} Contributions from the different pair potentials between the matrix and dimers in the ground and excited states cannot be neglected for these small values

TABLE V. Emission energies of dimer and trimer transitions in Ne, Ar, and Kr matrices. Gas phase values and matrix shifts, ΔE_m , are listed.

Excimer	Emission (eV)				$\Delta E_{em}/\text{meV}$		
	Gas	Ne	Ar	Kr	Ne	Ar	Kr
$\text{Ar}^+\text{F}^- (B)$	6.413	6.266	-150
$\text{Kr}^+\text{F}^- (B)$	5.00	4.83	-170
$\text{Kr}^+\text{F}^- (D)$	5.64	5.47	-170
Ar_2^+F^-	4.28	4.12	3.94		-160	-340	...
Kr_2^+F^-	3.10	2.88	2.82	2.73	-220	-280	-370

of ΔE_a . The inclusion of these effects would be necessary for a more quantitative discussion of the polarization effects.

Since the emissions are bound to free transitions which terminate on the repulsive part of the ground state potential, and the ground state vibrational bands are not resolved, the ΔE_{em} values in Table V correspond to the matrix shifts of the center of the emission bands. These ΔE_{em} values reflect the shift of the maximum of the Franck–Condon envelope and are more involved than the ΔE_a values because changes in the shapes and equilibrium positions of the potential surfaces by polarization effects become significant.³² A rearrangement of the matrix to accommodate the dipole moments of the B and D states could contribute a Stokes shift. These additional contributions can qualitatively account for the factor of 3 larger ΔE_{em} values compared to ΔE_a in Ne. An extensive investigation of the matrix effects on xenon hydrides³² showed that these effects scale linearly with ϵ . Given a mean value of $\Delta E_{em} = 300$ meV for Ar_2^+F^- and Kr_2^+F^- in Ar ($\epsilon = 1.66$) and scaled with a the ϵ dependent term $(\epsilon - 1)/(2\epsilon + 1)$ in Eq. (2), then ΔE_{em} values of 136 and 350 meV are derived for Ne and Kr ($\epsilon = 1.86$). This reflects the trends in Table V for the dimer and trimer emissions. An Onsager diameter of 7.4 Å, which is independent of dimer, trimer, or matrix, follows from this consideration. This is close to the reported values around 7 ± 5 Å.³² It should be indicated that this represents an oversimplification in view of the complexity of ΔE_{em} . A more involved discussion based on a modified Rittner potential^{17,33} should describe the vibrational energies, the anharmonicities (Table IV), the maxima of the Franck–Condon envelopes in absorption (Figs. 3 and 4), and the energy shifts in a consistent way. Such a treatment is out of the scope of this publication.

D. Lifetimes and stimulated emission cross sections

The dimer $B \rightarrow X$ transition is favorable for laser applications since the B state lies below the C and D states and is efficiently populated by nonradiative processes, as illustrated in Figs. 1(a) and 1(b). In addition, the cross section for stimulated emission, σ , scales inversely with the radiative lifetime, τ , and the spectral width of the emission band, $\Delta\nu$, according to

$$\sigma = \frac{\lambda^2}{8\pi n^2 \tau \cdot \Delta\nu} \quad (3)$$

and both τ and $\Delta\nu$ are small for the $B \rightarrow X$ transition (see Table I). In Eq. (3) the emission center wavelength is given by λ , and the refractive index of the matrix is given by n . The lifetimes for the $B \rightarrow X$ and $D \rightarrow X$ transitions are also listed in Table I. The measured lifetimes in the matrix, τ_m , must be corrected for the index of refraction of the matrix when compared to the gas phase. Using the standard assumption of a spherical cage for the depolarization factor³⁴ the gas phase lifetime τ_g is obtained by

$$\tau_g = \frac{\tau_m \cdot n \cdot (n^2 + 2)^2}{9}. \quad (4)$$

The comparison of corrected lifetimes, τ_g with the gas phase lifetimes τ , listed in Table I, yields a reasonable agreement. The cross sections, σ , calculated using the values of $\Delta\nu$ from Tables II and III, are of the order of 10^{-16} cm^2 . These large cross sections are typical for charge transfer transitions which have large dipole moments in the excited state.¹⁸ Stimulated emission may be obtained with high gain given a high density of the active species, and low transient absorption losses. This has been demonstrated in the case of XeF in Ar. Optical pumping of the KrF $B \rightarrow X$ transition in Ne can be accomplished by KrF (248 nm) and ArF (193 nm) gas phase lasers. The ArF excimer laser can pump the $D \rightarrow X$ emission as well. The $B \rightarrow X$ transition of ArF in Ne is too high in energy to be excited by the 193 nm ArF laser, but may be pumped by the F_2 laser at 157 nm. High power electron beam excitation of rare gas crystals has been demonstrated,³⁵ and energy transfer to the dopant may be an efficient pumping mechanism. The experience in Ref. 35 indicated a strong erosion of the Ne solid compared to the heavier rare gasses and this pumping scheme must be investigated in more detail.

V. CONCLUSIONS

Broadband irradiation of a sample of $F_2:\text{Ar}:\text{Ne}$ or $F_2:\text{Kr}:\text{Ne}$ forms argon fluoride or krypton fluoride species by the photodissociation of F_2 and subsequent mobility of fluorine atoms. Both dimer and trimer species are observed. Continuously tunable synchrotron radiation from the 3mNIM1 beamline is used to record excitation spectra over the range 50 to 300 nm. Emission spectra are recorded from 190 to 600 nm. Extended vibrational progressions of the B and D charge transfer states are observed in the excitation spectra of the ArF and KrF dimers in Ne matrices. Emission from both B and D states are observed for KrF, however only the B state emission is observed in ArF. The ArF D state emission is quenched by rapid relaxation into the B state. Emission and excitation spectra of the triatomic species Kr_2F and Ar_2F were recorded. The two bands observed in the Kr_2F excitation are assigned to $4^2\Gamma \leftarrow 1^2\Gamma$ and $5,6^2\Gamma \leftarrow 1^2\Gamma$, and similar assignments are expected for overlapping Ar_2F bands. Since only the $4^2\Gamma$ state of the triatomic charge transfer complex is bound, the emission is assigned to $4^2\Gamma \rightarrow 1,2^2\Gamma$.

The excitation and emission spectra of argon fluoride in an argon matrix are consistent with previous studies which identified Ar_2^+F^- and Ar_6^+F^- species. The excitation spec-

trum of krypton fluoride in the krypton matrix recorded in these studies is different from the previously reported spectra. A transient feature was observed near the krypton fluoride excitation which shows irradiation dependent photobleaching and recovery. This transient excitation feature is tentatively assigned to F atoms in an octahedral or tetrahedral interstitial site. A wavelength-dependent mechanism for the formation and depletion of these F atoms sites is used to account for the photobleaching and recovery.

To evaluate the utility of these cryogenic excimers as UV laser media, the lifetimes of the diatomic ArF and KrF emissions are measured and used to calculate the stimulated emission cross sections. The large stimulated emission cross sections ($\sim 10^{-16} \text{ cm}^2$) suggest that polycrystalline neon solids doped with ArF and KrF centers will make efficient lasers. A broadband incoherent source could be used to pump the ArF transition since the efficient relaxation of the excited state manifold exclusively populates the upper level of the lasing transition. Further experiments on optical and electron beam pumping of these systems will be considered.

ACKNOWLEDGMENTS

This work was supported by the Bundesminister für Bildung und Forschung via project 05 5KEAY B5 and by the Deutsche Forschungsgemeinschaft via Sonderforschungsbereich 337.

- ¹N. Schwentner and V. A. Apkarian, Chem. Phys. Lett. **154**, 413 (1989).
- ²G. Sliwinski and N. Schwentner, Appl. Phys. **B55**, 331 (1992).
- ³H. Kunttu, W. G. Lawrence, and V. A. Apkarian, J. Chem. Phys. **94**, 1692 (1991).
- ⁴A. I. Katz, J. Feld, and V. A. Apkarian, Opt. Lett. **19**, 441 (1989).
- ⁵G. Zerza, G. Sliwinski, and N. Schwentner, Appl. Phys. **A56**, 156 (1993).
- ⁶H. Kunttu, J. Feld, R. Alimi, A. Becker, and V. A. Apkarian, J. Chem. Phys. **92**, 4856 (1990).
- ⁷G. Zerza, Ph.D. thesis, Freie Universität Berlin, Germany, 1993.
- ⁸M. E. Fajardo and V. A. Apkarian, J. Chem. Phys. **85**, 5660 (1986).
- ⁹Excimer Lasers, 2nd edition, Vol. 30 of *Topics in Applied Physics*, edited by C. K. Rhodes (Springer, New York, 1984).
- ¹⁰J. Feld, H. Kunttu, and V. A. Apkarian, J. Chem. Phys. **93**, 1009 (1990).
- ¹¹H. Kunttu and V. A. Apkarian, Chem. Phys. Lett. **171**, 423 (1990).
- ¹²A. I. Krylov, R. B. Gerber, and V. A. Apkarian, Chem. Phys. **189**, 261 (1994).
- ¹³R. Alimi, R. B. Gerber, and V. A. Apkarian, J. Chem. Phys. **92**, 3551 (1990).
- ¹⁴C. Bressler and N. Schwentner, Phys. Rev. Lett. **22**, 648 (1996).
- ¹⁵B. S. Ault and L. Andrews, J. Chem. Phys. **65**, 4192 (1976).
- ¹⁶J. Goodman and L. E. Brus, J. Chem. Phys. **65**, 3808 (1976).
- ¹⁷G. Zerza, G. Sliwinski, N. Schwentner, G. J. Hoffmann, D. G. Imre, and V. A. Apkarian, J. Chem. Phys. **99**, 8414 (1993).
- ¹⁸T. H. Dunning and P. J. Hay, J. Chem. Phys. **69**, 134 (1978).
- ¹⁹P. J. Hay and T. H. Dunning, J. Chem. Phys. **69**, 2209 (1978).
- ²⁰W. R. Wadt and P. J. Hay, J. Chem. Phys. **68**, 3850 (1978).
- ²¹D. C. Heustis and N. E. Schlotter, J. Chem. Phys. **69**, 3100 (1978).
- ²²F. O. Ellison, J. Am. Chem. Soc. **69**, 3540 (1963).
- ²³C. Bressler, W. G. Lawrence, and N. Schwentner, J. Chem. Phys. **105**, 1318 (1996).
- ²⁴C. Bressler, W. G. Lawrence, and N. Schwentner, J. Chem. Phys. **102**, 48 (1995).
- ²⁵J. Bahrdt, P. Gürtler, and N. Schwentner, J. Chem. Phys. **86**, 6108 (1978).
- ²⁶J. E. Velazco, J. H. Kolts, and D. W. Setser, J. Chem. Phys. **65**, 3468 (1976).
- ²⁷H. Kunz, J. G. McCaffrey, M. Chergui, R. Schrieffer, Ö. Ünal, and N. Schwentner, J. Lumin. **48/49**, 621 (1991).

- ²⁸V. Aquilanti, E. Luzzatti, F. Pirani, and G. G. Volpi, *J. Chem. Phys.* **89**, 6165 (1988).
- ²⁹The vibrational energies of the ground state RgF potentials were calculated using a general one-dimension discrete variable representation algorithm based on a Leonard–Jones potential using the parameters in Ref. 28. See, for example, Z. Bacic and J. C. Light, *Annu. Rev. Phys. Chem.* **40**, 468 (1989).
- ³⁰D. C. McKean, *Spectrochim. Acta. Part A* **23**, 2405 (1967).
- ³¹H. Jara, H. Pummer, H. Egger, M. Shahidi, and C. K. Rhodes, *Phys. Rev. B* **34**, 7534 (1980).
- ³²M. Kraas, Ph.D. thesis, Hamburg, 1992.
- ³³E. S. Ritner, *J. Chem. Phys.* **19**, 1030 (1951).
- ³⁴T. Shibuya, *J. Chem. Phys.* **78**, 5175 (1983); *Chem. Phys. Lett.* **103**, 46 (1983).
- ³⁵H. Nahme and N. Schwentner, *Appl. Phys.* **B51**, 177 (1990).